EDGE ARTICLE

Check for updates

All publication charges for this article have been paid for by the Royal Society of Chemistry

Improving the interfacial stability of ultrahigh-nickel cathodes with PEO-based electrolytes by targeted chemical reactions†

Yuqing Dai,[a] Zihan Hou,[a] Gui Luo,[b] Duo Deng,[b] Wenjie Peng,[abc] Zhixing Wang,[ac] Huajun Guo,[ac] Xinhai Li,[ac] Guochun Yan,[ac] Hui Duan,[ac] Wenchao Zhang[ac] and Jiexi Wang 🔬 *[ac]

Benefiting from high energy density of ultrahigh-nickel cathode materials and good safety of PEO-based electrolytes, PEO-based ultrahigh-nickel solid-state lithium batteries (SLMBs) are considered to be new-generation energy storage devices. However, the incompatibility of ultrahigh-nickel cathode materials and PEO-based electrolytes is the main challenge due to serious interfacial side reactions. Therefore, the modification of the cathode/electrolyte interface is crucial. Herein, the residual lithium on the surface of $LiNi_{0.9}Co_{0.06}Mn_{0.04}O_2$ is utilized to construct an interfacial coating layer by reacting with H_3BO_3. The *in situ* formed $xLi_2O-B_2O_3$ coating layer (LBO1-NCM) with high ionic conductivity can be regulated with different crystal structures during the sintering process. Besides, an all-solid-state three-electrode cell is fabricated, which verifies that the $xLi_2O-B_2O_3$ coating can effectively stabilize the interface. Astonishingly, uneven Li anode deposition is observed in SLMBs, which is caused by the breakage of PEO molecular chains due to the strong oxidation of the cathode, while this crosstalk is also suppressed by the $xLi_2O-B_2O_3$ coating layer. Consequently, Li|PEO|LBO1-NCM achieves a substantially improved electrochemical performance, exhibiting 90.5% of capacity retention after 100 cycles for the coin cell and 80.3% of capacity retention after 200 cycles for the pouch cell. Apparently, the targeted modification of interfaces should be paid as much attention as electrolyte optimization in SLMBs.

1. Introduction

Solid-state lithium metal batteries (SLMBs) with high energy density and safety are one of the most promising energy storage devices.[1–3] Among multiple solid-state electrolytes, poly (ethylene oxide) (PEO)-based solid polymer electrolytes (SPEs) attract much attention due to their non-volatility, low flammability, good flexibility, simple manufacturing process, and excellent stability towards Li metal.[4–7] Consequently, they were first commercialized and used in electric vehicles.[8] Nevertheless, their further development is limited by low room-temperature ionic conductivity, which forces PEO-based SLMBs to operate with the assistance of external heat sources.[9]

To address the challenge mentioned above, many strategies focus on component optimization through polymer block copolymerization, blending, crosslinking, adding plasticizers, and adding inorganic fillers, thereby increasing the ionic conductivity to 10^{-4} S cm^{-1}.[10–18] In addition, there are many studies focusing on the optimization of anodes and detection technology.[19–21] On the other hand, it is crucial to choose a suitable cathode material to further improve the electrochemical performance of PEO-based SLMBs.[22] LiFePO$_4$ with stable electrochemical performance is usually used as the cathode and operates at a lower cut-off voltage (<4 V) to evaluate the practicality of the system, which makes it difficult to meet the pursuit of high energy density in batteries. Therefore, 4 V-class cathode materials such as LiCoO$_2$, LiNi$_x$Co$_y$Mn$_{1-x-y}$O$_2$, and spinel LiMn$_2$O$_4$ have been favored for SLMBs, but they all exhibit rapid capacity fading in PEO-based SLMBs.[23,24] Different decomposition and failure mechanisms with 4 V-class cathode materials have been reported in previous studies, which are briefly outlined in the following aspects. (1) Some studies emphasized that the rather high highest occupied molecular orbital (HOMO) of PEO leads to poor oxidative stability towards high voltage.[25] (2) Many researchers showed that even if the upper limit of the electrochemical stability windows (ESWs) of PEO is increased, there is still a rapid decline in electrochemical performance when matched with a high-voltage cathode.[26,27] (3) Some studies revealed that the strong oxidation of 4 V-class

ᵃEngineering Research Center of the Ministry of Education for Advanced Battery Materials, Hunan Provincial Key Laboratory of Nonferrous Value-Added Metallurgy, School of Metallurgy and Environment, Central South University, Changsha 410083, China. E-mail: wangjiexikeen@csu.edu.cn

ᵇBASF ShanShan Battery Material Co., Ltd, Changsha 410205, China

ᶜNational Engineering Research Centre of Advanced Energy Storage Materials, Changsha 410205, China

cathode materials at high voltage accelerates the decomposition of PEO, leading to self-oxygen loss and the consequent formation of the rock-salt phase of the high-nickel cathode.[28,29] Therefore, revealing the intensifying effect of 4 V-class cathode materials on PEO-based electrolyte decomposition and finding effective solutions is the key to achieving the stabilization of the cathode/electrolyte interface. Nevertheless, there is currently a lack of simple and direct electrochemical methods to reveal this phenomenon.

In this work, a solid-state three-electrode cell is designed to distinguish the impedance contributions of the anode and cathode and accurately monitor the changes in the cathode/electrolyte interfacial resistance, which reveals that the interface is stabilized by customized xLi$_2$O-B$_2$O$_3$ coating. Subsequently, the cycled SLMBs are disassembled to investigate the influence and mechanism of the xLi$_2$O-B$_2$O$_3$ coating on the ultrahigh-nickel cathode, PEO-based electrolyte, and Li anode. This indicates that the strong oxidation of ultrahigh-nickel cathode materials at high voltage accelerates the decomposition of PEO. Innovatively, this work effectively suppresses the electrochemical oxidation caused by a strong oxidizing cathode through targeted synthesis of the xLi$_2$O-B$_2$O$_3$ coating layer, instead of increasing the ESW of PEO, which is generally adopted by traditional methods. In addition, the inhibited PEO decomposition allows electrolytes to maintain sufficient mechanical strength to resist Li dendrites. Besides, this work reveals the intrinsic failure mechanism of ultrahigh-nickel cathodes matched with PEO-based electrolytes and testifies that the xLi$_2$O-B$_2$O$_3$ coating layer can effectively suppress structural degradation, achieving practical applications of SLMBs.

2. Results and discussion

The xLi$_2$O-B$_2$O$_3$ coated NCM materials were obtained by dispersing NMC and H$_3$BO$_3$ in NMP and then evaporating the NMP and sintering at 500 °C. The molar ratio of H$_3$BO$_3$/NCM (TM) is x: 10 000 (x = 0, 25, 50, 75), and the xLi$_2$O-B$_2$O$_3$ coated NCM materials were denoted as LBO0-NCM, LBO1-NCM, LBO2-NCM, and LBO3-NCM in order. To confirm the *in situ* formation of the coating layer on the surface of NCM particles, a series of characterization studies of pristine LBO0-NCM and LBO1-NCM were carried out. Scanning electron microscopy (SEM) images show that the surface morphology of all samples is micron-sized spherical secondary particles composed of nanograins (Fig. 1a and b, S1†). Moreover, there is no significant change in the morphology of the sample after coating. Besides, the surface of LBO1-NCM is smooth and clean, indicating that there is no uneven distribution of the coating material. Additionally, the elemental mapping areal scan images (Fig. 1c) also give the evenly distributed signals of elemental B on the surface of LBO1-NCM particles. X-ray diffraction (XRD) patterns of LBO0-NCM and LBO1-NCM reveal that the high-nickel cathode materials maintain their original layered structure with a space group of R-3m, which indicates that the LBO coating would not affect the phase composition of the pristine material (Fig. S2†). As shown in the high-resolution transmission electron microscope (HRTEM) images in Fig. 1d and e, the inner region (II) of LBO1-NCM is the same as that of LBO0-NCM (region (I)), both of which are layered phases (R-3m). A uniform coating layer with a thickness of approximately 10 nm can be observed on the surface of the LBO1-NCM particle. Moreover, there is no distinct delineation between the bulk and the coating layer, which is beneficial for good lattice matching to yield lower interface resistance. Furthermore, fast Fourier transformation (FFT) was performed on the selected area, and the corresponding crystal planes were determined by measuring the interplanar spacing and angle (Fig. 1f). The coating layer has multiple regions. Region III corresponds to LiBO$_2$, owing to the reaction between H$_3$BO$_3$ and residual lithium on the surface of the LBO1-NCM particle during the sintering process (reaction (1)). The
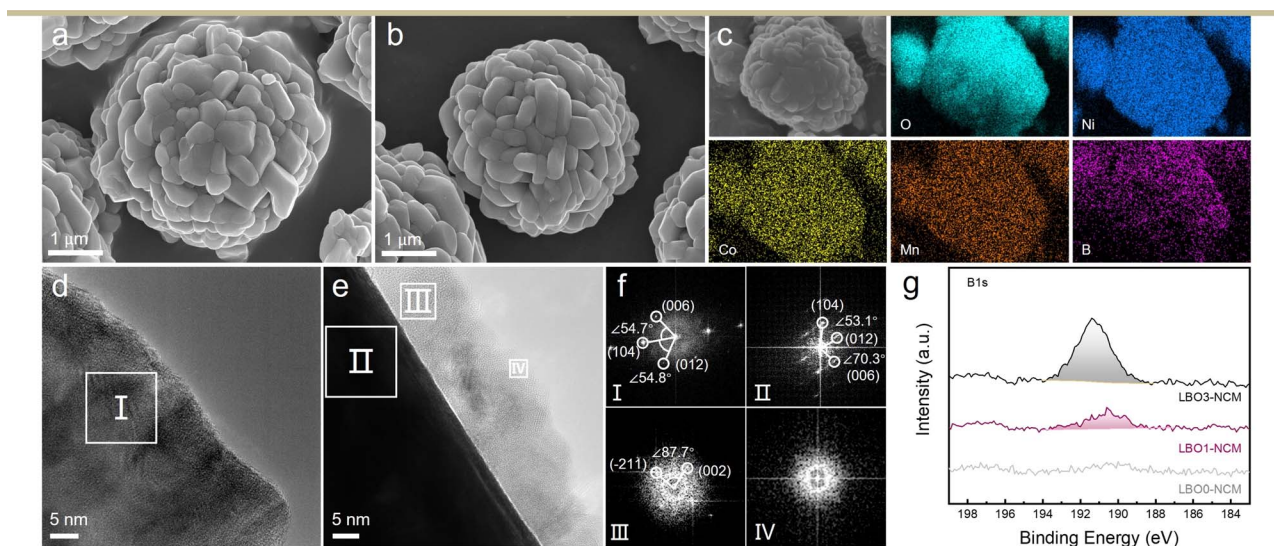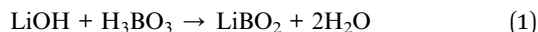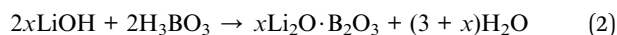

Fig. 1 SEM images of (a) LBO0-NCM and (b) LBO1-NCM. (c) Elemental mapping images of LBO1-NCM. HRTEM images of (d) LBO0-NCM and (e) LBO1-NCM. (f) Corresponding FFT patterns of areas I, II, III, and IV. (g) XPS spectra of LBO0-NCM, LBO1-NCM, and LBO3-NCM.

decrease in residual lithium content confirms the above results (Fig. S3†).

$$LiOH + H_3BO_3 \rightarrow LiBO_2 + 2H_2O \tag{1}$$

While the region IV is amorphous, corresponding to glassy $x\text{Li}_2\text{O-B}_2\text{O}_3$ ($x \geq 0$). Due to the continuous consumption of residual lithium on the surface, the outer layer of B_2O_3 and a small amount of remaining Li_2O are more easily melted, which is determined using the low melting point of B_2O_3. The phase diagram of Li_2O and B_2O_3 can explain this.[30] During the subsequent cooling process, the molten mixture forms glassy $x\text{Li}_2\text{O-B}_2\text{O}_3$ ($x \geq 0$) (reaction (2))

$$2x\text{LiOH} + 2\text{H}_3\text{BO}_3 \rightarrow x\text{Li}_2\text{O}\cdot\text{B}_2\text{O}_3 + (3 + x)\text{H}_2\text{O} \tag{2}$$

As shown in the result of X-ray photoelectron spectroscopy (XPS), a broad peak is observed in the spectra of B 1s, and the intensity increases with the increase of H_3BO_3 addition (Fig. 1g).[31] Presently, the accuracy of phase characterization of the coating layer is limited, and it is difficult to distinguish whether it is in a crystalline or glass state. Therefore, to obtain accurate characterization results, different mole ratios of H_3BO_3 and $LiOH \cdot H_2O$ were mixed and sintered under the same conditions as those of the coating process of the cathode materials. This can simulate the continuous reaction process between H_3BO_3 and $LiOH \cdot H_2O$ on the surface of the cathode material. Subsequently, XRD testing was performed on the sintered samples, and the results are shown in Fig. S4.† When there is a slight excess of $LiOH \cdot H_2O$, the sample mainly consists of crystal $LiBO_2$ and Li_3BO_3. When H_3BO_3 significantly exceeds, a broad peak appears at 22°, representing glassy $x\text{Li}_2\text{O-B}_2\text{O}_3$. Pure H_3BO_3 is glassy when sintered at 500 °C. This series of results simulated the continuous consumption of LiOH on the cathode materials surface, further confirming the various compounds ($x\text{Li}_2\text{O-B}_2\text{O}_3$) with crystalline inner and glassy outer layers.

Interfacial resistance is an important parameter for evaluating interfacial stability.[32] However, it is difficult to allocate the resistance to different interfaces due to the similar response frequencies.[33] To distinguish the impedance contributions of the anode and cathode and accurately monitor the changes in the cathode/electrolyte interfacial resistance, a three-electrode solid-state cell was established (Fig. 2a), where Li particles were placed as reference electrodes between two PEO separators. The all-solid-state three-electrode batteries were assembled with LBO0-NCM or LBO1-NCM as cathodes. The cells were activated at 0.1C for one cycle and then maintained for 10 hours at a voltage from 4.3 V to 4.7 V with a step range of 0.1 V (Fig. S5†). Electrochemical impedance spectroscopy (EIS) spectra were collected after every constant potential step to monitor the impedance growth during the operation of batteries under high-voltage conditions. The semi-circle in the high frequency range of the Nyquist plots is related to the interfacial resistance (R_{CEI}) between the cathode and electrolyte (Fig. S6†).[34] The fitting results of the R_{CEI} are shown in Fig. 2b. It shows a slight increase in R_{CEI} for both LBO0-NCM and LBO1-NCM during the constant potential step between 4.3 and 4.6 V, while the R_{CEI} maintains a lower value for LBO1-NCM. However, the R_{CEI} of LBO0-NCM rapidly increases to 688.9 Ω when the voltage reaches 4.7 V. Compared with pristine LBO0-NCM, the $x\text{Li}_2\text{O-B}_2\text{O}_3$ coating layer markedly reduced the R_{CEI} of LBO1-NCM due to the suppressed side reaction between the cathode and electrolyte. The EIS measurements in the three-electrode cell are applied as a convenient method to decouple the change of the impedance of the cathode/electrolyte interface at different voltages, intuitively showing the contribution of interfacial modification to the inhibition of side reactions.

To evaluate the effect of the $x\text{Li}_2\text{O-B}_2\text{O}_3$ coating layer, the electrochemical properties of PEO-based solid-state batteries were measured at room temperature (25 °C). As shown in Fig. 2c, after $x\text{Li}_2\text{O-B}_2\text{O}_3$, the initial capacities of the cathodes at 0.1C in 2.8–4.3 V gradually decrease from 218.2 mA h g^{-1} (LBO0-NCM) to 208.7 mA h g^{-1} (LBO3-NCM). This is because increasing the content of inactive $x\text{Li}_2\text{O-B}_2\text{O}_3$ results in a decrease in the active mass ratio in the cathode. Fig. 2d shows the cycling stability of these samples at 0.5C. The capacity retention of LBO1-NCM and LBO2-NCM after 100 cycles is 90.5% and 87.7%, respectively, much higher than that (78.3%) of LBO0-NCM. However, both the specific capacity and the capacity retention undergo a slight decrease in LBO3-NCM, owing to the obstructed transport of electrons caused by the thick $x\text{Li}_2\text{O-B}_2\text{O}_3$ coating layer. Therefore, the $x\text{Li}_2\text{O-B}_2\text{O}_3$ coating with suitable thickness would stabilize the interfacial reaction to improve the durability of specific capacity. The rate performance in Fig. 2e shows that the discharge capacity of LBO1-NCM (200.7 mA h g^{-1}) is lower than that of LBO0-NCM (207.9 mA h g^{-1}) at a low rate of 0.2C. With the continuous increase of the rate from 0.2C to 0.5C, 1C, and 2C, the discharge capacities decrease for both samples, and the capacities of LBO0-NCM exhibit a much faster decrease than that of LBO1-NCM. At 2C, the discharge capacity of LBO1-NCM is around 104.5 mA h g^{-1}, about 52.1% of the capacity at 0.2C, which is much higher than that of LBO0-NCM (71.1 mA h g^{-1}, 32.9%), LBO2-NCM (90.8 mA h g^{-1}, 43.2%), and LBO3-NCM (83.7 mA h g^{-1}, 40.2%). The direct current internal resistance (DCIR) method is often used as an easy and fast way to determine the cell resistance and the resistance build-up.[35,36] DCIR measurements were conducted by applying a 10 s long negative current pulse of 0.2C to the cell after a 20 min rest at OCV (open circuit voltage), corresponding to a change in SOC of 0.056%, which was considered to be negligible. The resistance was calculated from the difference between OCV and the potential at the end of the pulse (after 10 s) divided by the pulse current, as reported elsewhere.[37] The resistance of LBO0-NCM and LBO1-NCM at different states of charge (SOC) was collected and is shown in Fig. 2f. The $x\text{Li}_2\text{O-B}_2\text{O}_3$ coating layer significantly reduces the cell resistance, especially at 10% SOC, from 102.2 Ω of LBO0-NCM to 72.7 Ω of LBO1-NCM. Subsequently, the CV curves of the LBO0-NCM and LBO1-NCM samples are shown in Fig. S7.† Note that the CV curves of LBO1-NCM exhibit better reversibility compared to pristine LBO0-NCM after the first charge and discharge, implying that $x\text{Li}_2\text{O-B}_2\text{O}_3$ coatings
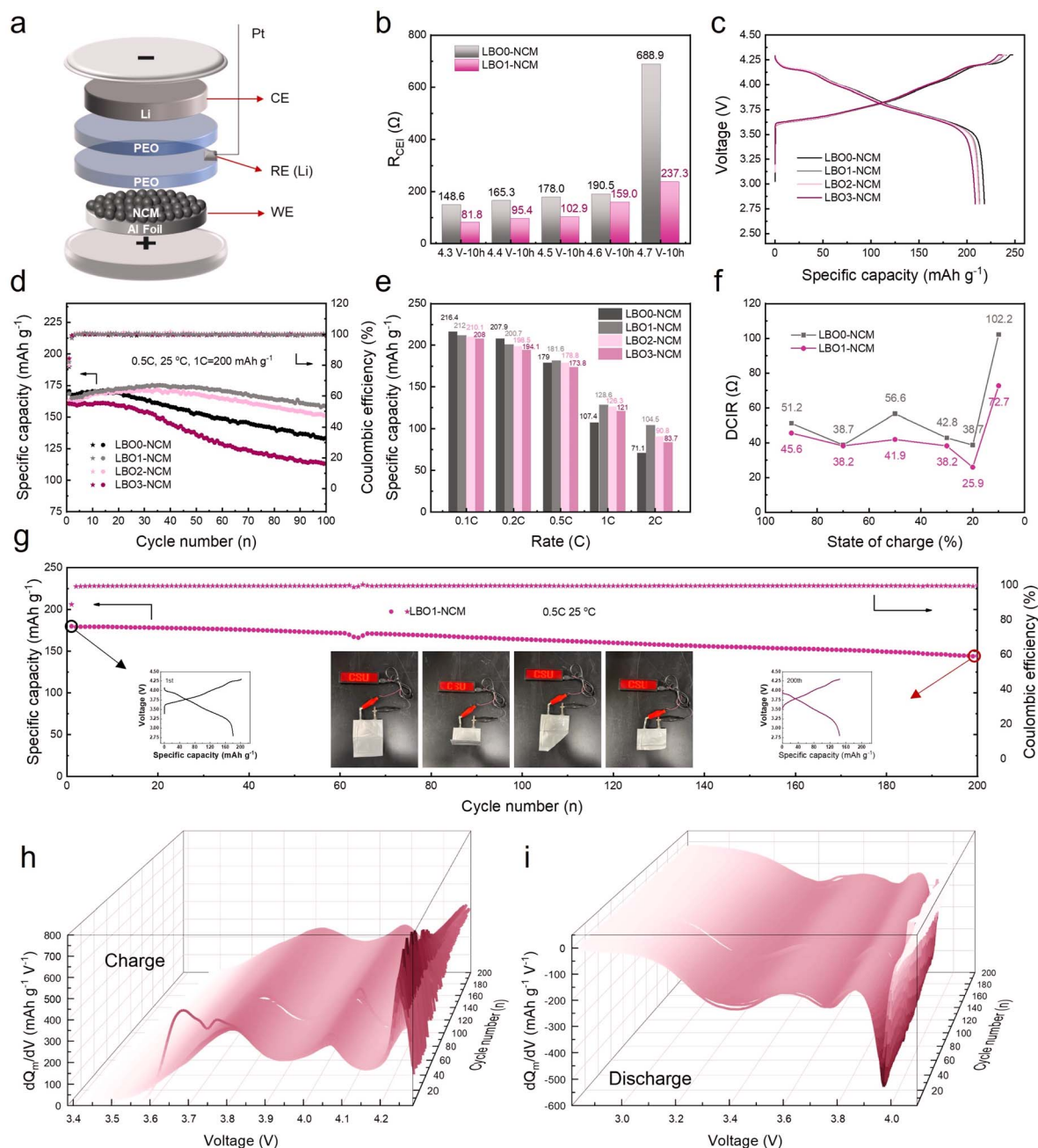
Fig. 2 (a) Schematic of the three-electrode PEO-based SLMB setup. (b) Corresponding fitting results of RCEI after 10 h of constant potential step at 4.3 V, 4.4 V, 4.5 V, 4.6 V and 4.7 V. (c) Initial charge/discharge curves at 0.1C. (d) Cycling performance and the corresponding coulombic efficiency at 0.5C. (e) Rate capability with different current densities of 0.1–2C. (f) The DCIR resistance of LBO0-NCM and LBO1-NCM at different SOC. (g) The cycling performances of the Li‖PEO‖LBO1-NCM pouch cell at 0.5C and the powering LED lamps test in as-prepared, bending, and cutting states. (h and i) Corresponding dQ/dV profiles of the Li‖PEO‖LBO1-NCM pouch cell at different electrochemical cycles.

improve the stability of the layered structure of the material. Besides, LBO1-NCM has the minimum ΔV (~198 mV, the voltage difference between oxidation and reduction peaks) due to the observably reduced polarization, which is beneficial for the enhancement of cycle reversibility and rate capability.

To certify the promising applicability of the ultrahigh-nickel cathode materials coated with xLi$_2$O-B$_2$O$_3$, Li|PEO|LBO1-NCM was also assembled and tested in the form of a pouch cell at around room temperature. As described in Fig. 2g, the initial

discharge capacity of the Li|PEO|LBO1-NCM pouch cell is 180.1 mA h g^{-1}. After 200 cycles at 0.5C, a remarkable reversible capacity of 144.6 mA h g^{-1} and an excellent capacity retention of 80.3% are achieved. In addition, the steady operation of Li|PEO|LBO1-NCM pouch cells under extreme circumstances is crucially important for the practical applications of SLMBs. Subsequently, the Li|PEO|LBO1-NCM pouch cell is tested in as-prepared, bending, and cutting states as illustrated in Fig. 2g. Notably, the brilliance of the light emitting diode (LED) lamp

matrix has no impact at all when it goes through bending. Even after cutting, the Li|PEO|LBO1-NCM pouch cell still works stably without short circuits, and the remaining portion can still light up the LED lamp matrix. Furthermore, with prolonging cycling numbers, no noticeable overpotential exists in the Li|PEO|LBO1-NCM pouch cell after 200 cycles as shown in Fig. S8,† suggesting that PEO-based electrolytes are highly stable at the interfaces between LBO1-NCM. Besides, such smooth charge–discharge curves indicate the cycled PEO-based electrolyte has robust mechanical strength to block Li dendrites.[38] To precisely probe the polarization evolution upon cycling, dQ/dV curves derived from the charge–discharge profiles are shown in Fig. 2h and i. The slight peak shift and relatively stable peak intensity of the redox reactions indicate the suppression of structure degradation and surface side reactions of LBO1-NCM that lead to the mitigation of capacity fading.

Based on the above results, the following speculation on the failure mechanism of PEO-based SLMBs with the ultrahigh-nickel cathode was proposed (Fig. 3a). In general, the reduction of a high-voltage cathode leads to its structural degradation and decomposition of PEO, resulting in capacity fade and large

polarization. Furthermore, PEO decomposition leads to molecular chain breakage, making it difficult to resist Li dendrites, which accelerates performance degradation. In contrast, the superior electrochemical stability of the xLi$_2$O-B$_2$O$_3$ coating layer suppresses the oxidative decomposition of PEO. To further confirm the effect of the xLi$_2$O-B$_2$O$_3$ coating on the SLMBs and its modification mechanism, the Li|PEO|LBO0-NCM and Li|PEO|LBO1-NCM cells were disassembled after cycling and the cathode, PEO-based electrolyte and anode were characterized separately. Fig. 3b and c show the particle morphology of the pristine LBO0-NCM and LBO1-NCM after 100 cycles. Note that there is a thick cathode-electrolyte interphase (CEI) in pristine LBO0-NCM, which is caused by the continuous decomposition of PEO due to the strong oxidizability of Ni^{3+} and Ni^{4+} during the charging and discharging process.[27,28] Nevertheless, LBO1-NCM shows a thin and smooth CEI, indicating that the xLi$_2$O-B$_2$O$_3$ coating effectively improves the stability of the interface between the cathode and PEO-based electrolyte. XPS spectra of the PEO-based electrolyte after 100 cycles in Li|PEO|LBO0-NCM and Li|PEO|LBO1-NCM are shown in Fig. 3d and e. The peaks at 286.6 eV and 284.8 eV in the C 1s spectra can be assigned to the C–O and C–C/
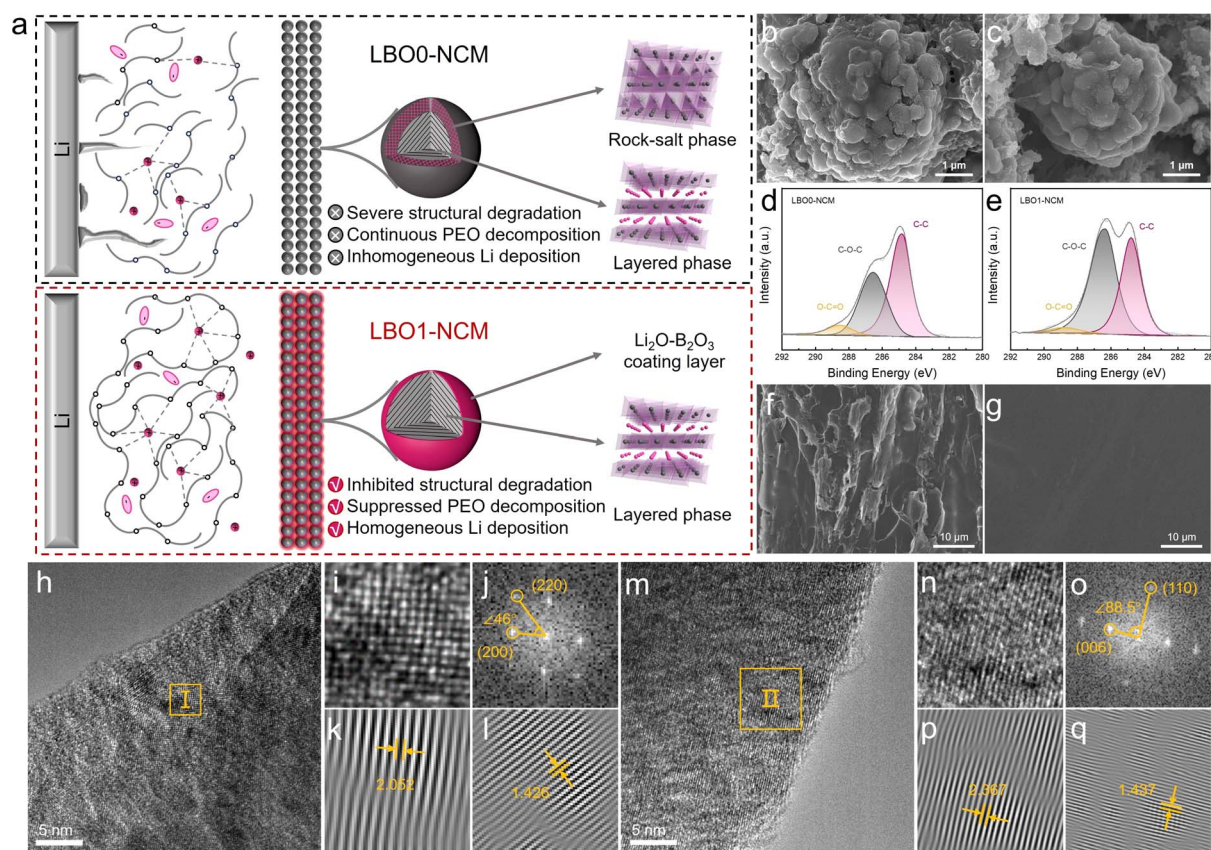

Fig. 3 (a) Mechanism diagram of property enhancement. The SEM images of (b) LBO0-NCM and (c) LBO1-NCM after 100 cycles. The XPS spectra of C 1s of PEO after 100 cycles in (d) Li||PEO||LBO0-NCM and (e) Li||PEO||LBO1-NCM. The SEM images of the disassembled-lithium metal after 100 cycles in (f) Li||PEO||LBO0-NCM and (g) Li||PEO||LBO1-NCM. (h) High-resolution TEM images of particles acquired from cycled LBO0-NCM. (i) The larger version of area I in (h). (j) The corresponding FFT patterns and (k and l) inverse FFT patterns of area I in (h). (m) High-resolution TEM images of particles acquired from cycled LBO1-NCM. (n) The larger version of area II in (m). (o) The corresponding FFT patterns and (p and q) inverse FFT patterns of area II in (m).
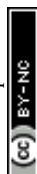
C–H bonds of PEO.[38,39] Obviously, taking the stable peak of C–C/C–H as a reference, the C–O peak area of PEO in Li|PEO|LBO0-NCM is significantly lower than that of Li|PEO|LBO1-NCM, indicating the severe decomposition of the C–O bond in PEO when matched with unmodified LBO0-NCM, which is caused by the low ESW of C–O and the strong oxidation of ultrahigh-nickel cathode materials at high voltage.[28,40] In addition, the high-voltage cathode further intensifies its decomposition. The decomposition of C–O bonds generally leads to the breakage of PEO molecular chains, which reduces the mechanical strength of PEO-based electrolytes. However, the decomposition of C–O in Li|PEO|LBO1-NCM is significantly inhibited, which is attributed to the physical isolation between the ultrahigh-nickel cathodes and PEO by xLi$_2$O-B$_2$O$_3$ coating. Besides, many studies have mentioned that xLi$_2$O-B$_2$O$_3$ has low electronic conductivity.[41–43] Coating cathode materials with xLi$_2$O-B$_2$O$_3$ can prevent electron transfer between the cathode and electrolyte, thus inhibiting the electrochemical oxidation of electrolytes. The additional peak after electrochemical cycling would be expected in the spectral region between 288.3 eV which corresponds to the C=O assigned to the carbonyl functional groups of aldehyde, ketone, or ester species, indicating oxidative decomposition processes of PEO.[38] Similarly, a lower C=O peak indicates that the xLi$_2$O-B$_2$O$_3$ coated cathode materials suppresses the oxidative decomposition of PEO.

To further validate the improved Li dendrite blocking ability, the morphology of the cycled Li anodes in Li|PEO|LBO0-NCM and Li|PEO|LBO1-NCM was carefully scrutinized by SEM as illustrated in Fig. 3f and g. For comparison, the cycling performance of Li|PEO|LFP with LiFePO$_4$ as cathode materials was also tested using the same charging and discharging procedure and the Li anode was scrutinized by SEM (Fig. S9†). Apparently, the after-cycling surface of the Li anode in Li|PEO|LFP is still flat and smooth without Li dendrites (Fig. S10†). Conversely, a significant number of Li dendrites resulting from inhomogeneous Li deposition can be observed on the surface of the Li anode after cycling in Li|PEO|LBO0-NCM. This is because of the severe decomposition of C–O–C bonds in PEO caused by the strong oxidizability Ni^{3+}/Ni^{4+} on the surface of the ultrahigh-nickel cathode, leading to the breakage of PEO molecular chains. Thereby the decreased mechanical strength eventually reduces its ability to suppress uneven Li deposition.[44–46] Satisfactorily, the Li anode in Li|PEO|LBO1-NCM recovers smoothly after coating the cathode with xLi$_2$O-B$_2$O$_3$, owing to the inhibited decomposition of PEO by the coating layer due to its low electrical conductivity. Such comparative experiments prove that the decomposition of PEO is mainly caused by the direct chemical decomposition of highly oxidizing ultra-high nickel cathodes rather than simple electrochemical decomposition at high voltage limited by its low
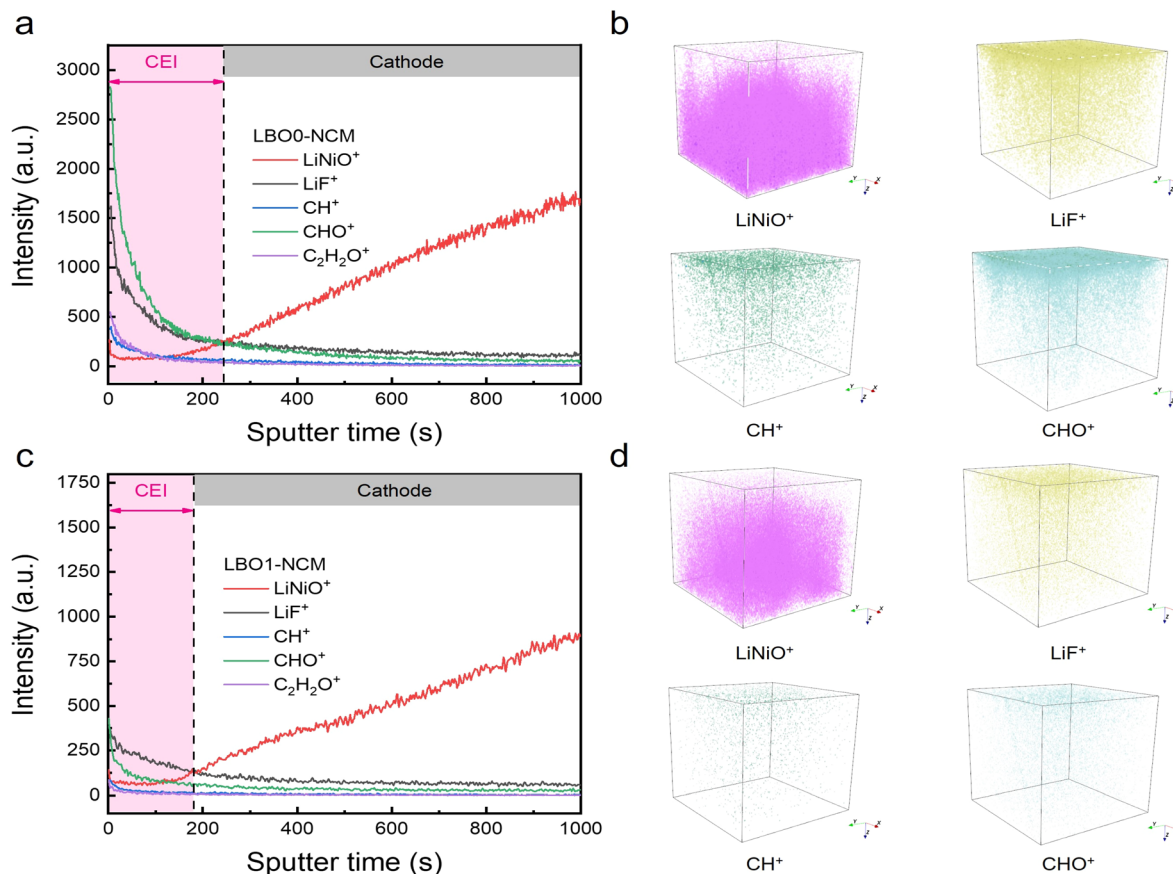

Fig. 4 (a) ToF-SIMS depth profiles and (b) corresponding 3D spatial distributions of the representative fragments across the LBO0-NCM cathode. (c) ToF-SIMS depth profiles and (d) corresponding 3D spatial distributions of the representative fragments across the LBO1-NCM cathode.

ESW, which will also affect the uniformity of Li deposition. Fortunately, this work confirms that the xLi$_2$O-B$_2$O$_3$ coating layer with low electrical conductivity can effectively solve the above problems.

To deeply understand the influence of the xLi$_2$O-B$_2$O$_3$ coating layer on the surface species and crystalline structure of ultrahigh-nickel cathode particles, HRTEM after cycling was conducted. FFT was performed on the selected area, and the corresponding crystal planes were determined by measuring the interplanar spacing and angle. As shown in Fig. 3h–l, LBO0-NCM after 100 cycles exhibits the NiO rock-salt phase $Fm3m$ with a thickness of 5–8 nm on the surface (I). The formation of the surface NiO rock-salt phase can be attributed to PEO oxidation, which will block the Li$^+$ diffusion pathway to a great extent within the ab-plane.[47] During the charging process, the partial Ni^{4+} turns to Ni^{3+} due to the reducibility of PEO, which reduces the formation energy of oxygen vacancies and thus drives lattice oxygen release. As such, a rock-salt phase is formed on the cathode surface.[23,48] In brief, the fast capacity fading of LBO0-NCM in SLMBs is related to the formation of the rock-salt phase led by PEO corrosion.[28] In contrast, there are no significant differences between the surface regions and the bulk of cycled LBO1-NCM (Fig. 3m–q), which still exhibit layered $R\bar{3}m$ structures, because the irreversible phase transformation can be mitigated by xLi$_2$O-B$_2$O$_3$ coating due to the enhanced cathode/electrolyte compatibility. As discussed above, the enhanced ion transport capability and superior interfacial stability of the xLi$_2$O-B$_2$O$_3$ coating layer boost the electrochemical performance toward practical applications.

Furthermore, TOF-SIMS was carried out to elucidate the composition and structure of the CEI on the cathode surface in a three-dimensional distribution. As shown in Fig. 4, the thickness of the CEI derived by LBO1-NCM is thinner than that by LBO0-NCM, which is identified using the intensity of LiF$^+$ and LiNiO$^+$ fragments and calibrated using the GaN sputtering rate. In addition, compared with LiNiO$^+$ representing cathode materials, the signals of LiF$^+$, CH$^+$, CHO$^+$, and C$_2$H$_2$O$^+$ representing electrolyte and lithium salt decomposition in LBO1-NCM are significantly lower than those in LBO0-NCM. Therefore, the TOF-SIMS results further confirmed that a thick CEI in pristine LBO0-NCM, and xLi$_2$O-B$_2$O$_3$ coated LBO1-NCM materials significantly inhibited the formation of interface side reaction products.

3. Conclusion

In summary, we have synthesized an ultrahigh-nickel cathode material where NCM nanoparticles are well-wrapped with high ionic conductivity xLi$_2$O-B$_2$O$_3$ by *in situ* target chemical reactions. Besides, an all-solid-state three-electrode battery was fabricated to decouple the impedance changes at the cathode/electrolyte interface and evaluate the effectiveness of the xLi$_2$O-B$_2$O$_3$ coating layer on cathode materials. Our research indicated that the poor electrochemical performances of Li|PEO|LBO0-NCM originated from the high oxidizing ability of NCM at high voltages, which not only accelerates the decomposition of PEO but also drives the self-oxygen-release of NCM.

Furthermore, the breakage of PEO molecular chains reduced the mechanical strength of solid-state electrolytes, which led to inhomogeneous Li deposition. Fortunately, the xLi$_2$O-B$_2$O$_3$ coating layer with low electrical conductivity was confirmed to prevent interface side reactions and significantly improved cycle stability and rate performance of the SLMBs. The steady operation of the Li|PEO|LBO1-NCM pouch cell under extreme circumstances indicated the applicable potential of the proposed solid batteries. As a vision, the targeted modification of the interface between electrolyte and the electrode, rather than the stability of solid-state electrolyte itself, is a more momentous and noteworthy issue in the design of SLMBs.

4. Experimental section

4.1 Preparation of cathodes and electrolytes

Firstly, NCM was prepared by mixing precursor Ni$_{0.90}$Co$_{0.06}$Mn$_{0.04}$(OH)$_2$ (BASF Shanshan Battery Materials Co. Ltd.) and LiOH·H$_2$O (BASF Shanshan Battery Materials Co. Ltd) in an agate mortar, and the molar ratio of Li/transition metal (TM) is 1 : 1.05. The mixture was then calcined at 500 °C for 3 h followed by 750 °C for 12 h in an oxygen atmosphere. Secondly, 2 g NCM was mixed with 5 mL NMP and stirred for 10 min. Then, H$_3$BO$_3$ (Aladdin, 99.99% metal basis) was added to this mixture and stirred for 20 min, and the molar ratio of H$_3$BO$_3$/NCM (TM) is x: 10 000 ($x = 0, 25, 50, 75$). Finally, the slurry was vacuum dried at 90 °C for 12 h and then calcined at 500 °C for 5 h in an oxygen atmosphere. The products were named LBO0-NCM, LBO1-NCM, LBO2-NCM, and LBO3-NCM, respectively. LBOx-NCM, Super P, and PVDF were dissolved in NMP with a mass ratio of 80 : 10 : 10, then they were evenly mixed and coated on an Al current collector, and then heated at 90 °C for 4 h under vacuum. The dried electrodes were cut into round pieces (Φ12 mm, with ~2 mg cm^{-2} loading weight). Lithium metal (Φ14 mm) was chosen as the anode for the coin cell, and a 25 μm lithium strip was chosen as the anode for the pouch cell. To prepare PEO-based electrolyte, 0.2175 g LiTFSI (Duoduo Chemical Technology Co. Ltd.), 0.05 g LiDFOB (Duoduo Chemical Technology Co. Ltd.), and 0.15 g TEGDME (Macklin, 99%) were mixed with 15 mL acetonitrile (AN, Aladdin, 99.5%) and stirred for 2 h. Subsequently, PEO (EO : LiTFSI = 15 : 1) was added to this mixture and stirred for 24 h to get a gel-like slurry. Then, the slurry was poured into a Teflon gasket and dried at room temperature to obtain the polymer solid electrolyte membrane. When assembling the batteries in 2025-type coin cells and pouch cells, H$_2$O and O$_2$ contents in the glovebox were both controlled at less than 0.1 ppm.

4.2 Material characterization

The crystal structure of the samples was identified by XRD with Cu Kα using an Empyrean 2 (PANalytical). SEM (JSM-7610F, JEOL) and TEM (Titan G2, FEI) were applied to characterize the morphology and microstructure of samples. The chemical status of the cathodes after cycling was characterized by XPS (PHI VersaProbe 4, ULVAC-PHI). TOF-SIMS (TOF.SIMS5-100)

was carried out to characterize CEI distribution, and the test area was 100×100 µm.

4.3 Electrochemical characterization

EIS curves were tested using a Bio-Logic SP150 in the frequency range from 1 M Hz to 0.01 Hz with a perturbation amplitude of 10 mV. Charge–discharge tests of all samples were performed on a NEWARE battery test system with a voltage range from 2.8 to 4.3 V. The activation process was initially conducted for two cycles at 0.1C for both the charge and discharge processes. The cycling and rate performance were tested at a charging current of 0.2C. CV measurements of ASSBs were performed using a CHI660D electrochemical workstation in the voltage range between 2.8 and 4.3 V with a scanning speed of 0.05 mV s^{-1}. The DCIR was tested on the NEWARE battery test system at 0.2C. The Li$^+$ chemical diffusion coefficients (D_{Li^+}) were determined using the galvanostatic intermittent titration technique (GITT), which was performed at 0.1C for 30 min of charging, followed by 1 h of relaxation between 2.8 and 4.3 V. All the above tests were conducted at 25 °C.

Data availability

The authors state that the data are available on request.

Author contributions

Yuqing Dai: conceptualization, formal analysis, validation, investigation, and writing – original draft. Zihan Hou: writing – original draft. Gui Luo, Duo Deng, and Wenjie Peng: resources and funding acquisition. Zhixing Wang, Huajun Guo, Xinhai Li, Guochun Yan, and Wenchao Zhang: funding acquisition and writing – review & editing. Hui Duan: supervision and writing – review & editing. Jiexi Wang: conceptualization, supervision, funding acquisition, and writing – review & editing.

Conflicts of interest

There are no conflicts to declare.

Acknowledgements

Notes and references

1 L. Wu, F. Pei, D. Cheng, Y. Zhang, H. Cheng, K. Huang, L. Yuan, Z. Li, H. Xu and Y. Huang, *Adv. Funct. Mater.*, 2023, 2310084.

2 W. Li, J. A. Quirk, M. Li, W. Xia, L. M. Morgan, W. Yin, M. Zheng, L. C. Gallington, Y. Ren, N. Zhu, G. King, R. Feng, R. Li, J. A. Dawson, T.-K. Sham and X. Sun, *Adv. Mater.*, 2023, **36**, 2302647.

3 P. Prakash, B. Fall, J. Aguirre, L. A. Sonnenberg, P. R. Chinnam, S. Chereddy, D. A. Dikin, A. Venkatnathan, S. L. Wunder and M. J. Zdilla, *Nat. Mater.*, 2023, **22**, 627–635.

4 D. Ding, H. Ma, H. Tao, X. Yang and L.-Z. Fan, *Chem. Sci.*, 2024, **15**, 3730–3740.

5 S. Kim, H. J. Kim, H. Yashiro, N. Voronina and S.-T. Myung, *Chem. Eng. J.*, 2024, **480**, 148254.

6 R. Fang, B. Xu, N. S. Grundish, Y. Xia, Y. Li, C. Lu, Y. Liu, N. Wu and J. B. Goodenough, *Angew. Chem., Int. Ed.*, 2021, **60**, 17701–17706.

7 H. Zhou, H. Liu, X. Xing, Z. Wang, S. Yu, G. M. Veith and P. Liu, *Chem. Sci.*, 2021, **12**, 7023–7032.

8 Z. Song, F. Chen, M. Martinez-Ibanez, W. Feng, M. Forsyth, Z. Zhou, M. Armand and H. Zhang, *Nat. Commun.*, 2023, **14**, 4884.

9 L. Liu, T. Wang, L. Sun, T. Song, H. Yan, C. Li, D. Mu, J. Zheng and Y. Dai, *Energy Environ. Mater.*, 2024, **7**, e12580.

10 J. Kang, Z. Yan, L. Gao, Y. Zhang, W. Liu, Q. Yang, Y. Zhao, N. Deng, B. Cheng and W. Kang, *Energy Storage Mater.*, 2022, **53**, 192–203.

11 B. Luo, J. Wu, M. Zhang, Z. Zhang, X. Zhang, Z. Fang, Z. Xu and M. Wu, *Chem. Sci.*, 2023, **14**, 13067–13079.

12 H. Jamal, F. Khan, H. Lim and J. H. Kim, *Sustainable Mater. Technol.*, 2023, **35**, e00548.

13 G. Lingua, P. Grysan, P. S. Vlasov, P. Verge, A. S. Shaplov and C. Gerbaldi, *Macromolecules*, 2021, **54**, 6911–6924.

14 J. Rolland, J. Brassinne, J. P. Bourgeois, E. Poggi, A. Vlad and J. F. Gohy, *J. Mater. Chem. A*, 2014, **2**, 11839–11846.

15 X. Zhan, M. Li, X. Zhao, Y. Wang, S. Li, W. Wang, J. Lin, Z.-A. Nan, J. Yan, Z. Sun, H. Liu, F. Wang, J. Wan, J. Liu, Q. Zhang and L. Zhang, *Nat. Commun.*, 2024, **15**, 1056.

16 G. Yang, M. L. Lehmann, S. Zhao, B. Li, S. Ge, P.-F. Cao, F. M. Delnick, A. P. Sokolov, T. Saito and J. Nanda, *Energy Storage Mater.*, 2021, **35**, 431–442.

17 J. Peng, L.-N. Wu, J.-X. Lin, C.-G. Shi, J.-J. Fan, L.-B. Chen, P. Dai, L. Huang, J.-T. Li and S.-G. Sun, *J. Mater. Chem. A*, 2019, **7**, 19565–19572.

18 B. Jin, D. Wang, Y. He, J. Mao, Y. Kang, C. Wan, W. Xia, J. Kim, M. Eguchi and Y. Yamauchi, *Chem. Sci.*, 2023, **14**, 7956–7965.

19 X. Han, L. Gu, Z. Sun, M. Chen, Y. Zhang, L. Luo, M. Xu, S. Chen, H. Liu, J. Wan, Y.-B. He, J. Chen and Q. Zhang, *Energy Environ. Sci.*, 2023, **16**, 5395–5408.

20 Z. Sun, Q. Yin, H. Chen, M. Li, S. Zhou, S. Wen, J. Pan, Q. Zheng, B. Jiang, H. Liu, K. Kim, J. Li, X. Han, Y.-B. He, L. Zhang, M. Li and Q. Zhang, *Interdiscip. Mater.*, 2023, **2**, 635–663.

21 Z. Sun, J. Pan, W. Chen, H. Chen, S. Zhou, X. Wu, Y. Wang, K. Kim, J. Li, H. Liu, Y. Yuan, J. Wang, D. Su, D.-L. Peng and Q. Zhang, *Adv. Energy Mater.*, 2024, **14**, 2303165.

22 X. Tang, X. Xu, M. Bai, M. Zhang, H. Wang, Z. Wang, A. Shao, H. Wang and Y. Ma, *Adv. Funct. Mater.*, 2023, **33**, 2210465.

23 R. Huang, Y. Ding, F. Zhang, W. Jiang, C. Zhang, P. Yan, M. Ling and H. Pan, *J. Energy Chem.*, 2022, **75**, 504–511.

24 S. Li, K. Huang, L. Wu, D. Xiao, J. Long, C. Wang, H. Dou, P. Chen and X. Zhang, *Chem. Sci.*, 2023, **14**, 10786–10794.

25 N. Wang, Y. An and S. Wang, *Chem. Commun.*, 2023, **59**, 334–337.

26 T. M. Nguyen, D. W. Kim, D. Y. Kim, G. Choi, J. Suk and Y. Kang, *ACS Appl. Energy Mater.*, 2022, **5**, 15768–15779.

27 H. J. Guo, H. X. Wang, Y. J. Guo, G. X. Liu, J. Wan, Y. X. Song, X. A. Yang, F. F. Jia, F. Y. Wang, Y. G. Guo, R. Wen and L. J. Wan, *J. Am. Chem. Soc.*, 2020, **142**, 20752–20762.

28 M. Yi, J. Li, M. Wang, X. Fan, B. Hong, Z. Zhang, Z. Zhang, H. Jiang, A. Wang and Y. Lai, *Energy Storage Mater.*, 2023, **54**, 579–588.

29 X. Pan, H. Sun, Z. Wang, H. Huang, Q. Chang, J. Li, J. Gao, S. Wang, H. Xu, Y. Li and W. Zhou, *Adv. Energy Mater.*, 2020, **10**, 2002416.

30 B. S. R. Sastry and F. A. Hummel, *J. Am. Ceram. Soc.*, 1958, **41**, 7–17.

31 B. You, Z. Wang, Y. Chang, W. Yin, Z. Xu, Y. Zeng, G. Yan and J. Wang, *Fundam. Res.*, 2023, **3**, 618–626.

32 Y. Yusim, D. F. Hunstock, A. Mayer, D. Bresser, S. Passerini, J. Janek and A. Henss, *Adv. Mater. Interfaces*, 2024, **11**, 2300532.

33 V. Wurster, C. Engel, H. Graebe, T. Ferber, W. Jaegermann and R. Hausbrand, *J. Electrochem. Soc.*, 2019, **166**, A5410–A5420.

34 Q. Guo, J. Zheng, Y. Zhu, H. Jiang, H. Jiang, H. Wang, W. Sun, H. Sang, Y. Han, C. Zheng and K. Xie, *Energy Storage Mater.*, 2022, **48**, 205–211.

35 T. Teufl, D. Pritzl, S. Solchenbach, H. A. Gasteiger and M. A. Mendez, *J. Electrochem. Soc.*, 2019, **166**, A1275–A1284.

36 R. Xu, D. Wang, G. Yan, J. Duan, H. Guo, J. Wang, Z. Wang, X. Li and G. Li, *J. Energy Storage*, 2023, **70**, 108100.

37 H.-G. Schweiger, O. Obeidi, O. Komesker, A. Raschke, M. Schiemann, C. Zehner, M. Gehnen, M. Keller and P. Birke, *Sensors*, 2010, **10**, 5604–5625.

38 Y. Yusim, E. Trevisanello, R. Ruess, F. H. Richter, A. Mayer, D. Bresser, S. Passerini, J. Janek and A. Henss, *Angew. Chem., Int. Ed.*, 2023, **62**, e202218316.

39 H. Yan, T. Wang, L. Liu, T. Song, C. Li, L. Wu, J.-C. Zheng and Y. Dai, *J. Power Sources*, 2023, **557**, 232559.

40 X. Yang, M. Jiang, X. Gao, D. Bao, Q. Sun, N. Holmes, H. Duan, S. Mukherjee, K. Adair, C. Zhao, J. Liang, W. Li, J. Li, Y. Liu, H. Huang, L. Zhang, S. Lu, Q. Lu, R. Li, C. V. Singh and X. Sun, *Energy Environ. Sci.*, 2020, **13**, 1318–1325.

41 B. Zhang, J. Shen, Q. Wang, C. Hu, B. Luo, Y. Liu, Z. Xiao and X. Ou, *Energy Environ. Mater.*, 2022, e12270.

42 Y. Xia, A. Chen, K. Wang, Q. Mao, H. Huang, J. Zhang, X. He, Y. Gan, Z. Xiao and W. Zhang, *Chem. Eng. J.*, 2022, **450**, 138382.

43 X. Tang, Q. Jia, L. Yang, M. Bai, W. Wu, Z. Wang, M. Gong, S. Sa, S. Tao, M. Sun and Y. Ma, *Energy Storage Mater.*, 2020, **33**, 239–249.

44 Y. Xia, Q. Wang, Q. Liu, J. Zhang, X. Xia, H. Huang, Y. Gan, X. He, Z. Xiao and W. Zhang, *J. Colloid Interface Sci.*, 2023, **638**, 908–917.

45 Q. Wu, M. Fang, S. Jiao, S. Li, S. Zhang, Z. Shen, S. Mao, J. Mao, J. Zhang, Y. Tan, K. Shen, J. Lv, W. Hu, Y. He and Y. Lu, *Nat. Commun.*, 2023, **14**, 6296.

46 T. Zhu, G. Q. Liu, D. L. Chen, J. X. Chen, P. Qi, J. Sun and S. Zhang, *Energy Storage Mater.*, 2022, **50**, 495–504.

47 S. Li, Z. Yao, J. Zheng, M. Fu, J. Cen, S. Hwang, H. Jin, A. Orlov, L. Gu, S. Wang, Z. Chen and D. Su, *Angew. Chem., Int. Ed.*, 2020, **59**, 22092–22099.

48 C. Sun, X. Liao, F. Xia, Y. Zhao, L. Zhang, S. Mu, S. Shi, Y. Li, H. Peng, G. Van Tendeloo, K. Zhao and J. Wu, *ACS Nano*, 2020, **14**, 6181–6190.